npj | climate and atmospheric science

Article

Published in partnership with CECCR at King Abdulaziz University

https://doi.org/10.1038/s41612-025-01144-3

How to think about the clear-sky shortwave water vapor feedback

Florian E. Roemer[1,3] ✉, Stefan A. Buehler[1] & Kaah P. Menang[1,2]

Earth's climate feedback quantifies the response of Earth's energy budget to temperature changes and thus determines climate sensitivity. The climate feedback is largely controlled by water vapor which absorbs both longwave radiation emitted by Earth and shortwave radiation from the Sun. For the clear-sky shortwave water vapor feedback λ_{SW}, a gap remains between process understanding and estimates from comprehensive climate models. Therefore, we present a hierarchy of simple models for λ_{SW}. We show that λ_{SW} is proportional to the change with temperature in the square of atmospheric transmissivity that depends on the atmospheric concentration of water vapor and its ability to absorb shortwave radiation. The global mean λ_{SW} is well captured by a simple analytical model that approximates the strong spectral variations in water vapor absorption, whereas its temperature dependence results from spectral details in water vapor absorption. With this study, we expand the conceptual understanding of an important but understudied feedback component.

Water vapor is the most important greenhouse gas in Earth's atmosphere. In particular, it strongly absorbs terrestrial radiation and thus reduces the magnitude of the longwave feedback by roughly a factor of two [e.g., refs. 1,2]. However, water vapor also absorbs solar radiation and thus causes a corresponding shortwave water vapor feedback. At the same time, conceptual and analytical studies to understand the effect of water vapor have so far been limited to the longwave feedback [e.g., refs. 3–6]. To close this gap, we present a hierarchy of simple analytical and numerical models to study the clear-sky shortwave water vapor feedback.

The main mechanism of the shortwave water vapor feedback is the same as for the longwave, resulting from two well-understood properties of water vapor. First, water vapor effectively absorbs both terrestrial and solar radiation, and second, its concentration increases with warming following the Clausius-Clapeyron relation. Hence, water vapor absorption increases with temperature. However, there is one important difference between the longwave and shortwave water vapor feedbacks: The longwave water vapor feedback is closely linked to changes in longwave thermal emission [e.g., refs. 3,7], whereas shortwave thermal emission is generally negligible in Earth's atmosphere. Following common practice [e.g., ref. 8], we thus define shortwave radiation as radiation originating from the Sun in the spectral range 2000–32000 cm^{-1} that encompasses 98% of the total solar irradiance.

Although the shortwave water vapor feedback originates from clear-sky processes, its magnitude is substantially affected by the presence of clouds: The global mean shortwave water vapor feedback is estimated at around 0.16 $W\,m^{-2}\,K^{-1}$ in clear-sky conditions, but its magnitude increases to 0.25–0.3 $W\,m^{-2}\,K^{-1}$ under all-sky conditions [e.g., refs. 9–11]. This is because cloud particles scatter shortwave radiation which increases its path length in Earth's atmosphere and thus enhances the effect of water vapor absorption[9]. However, this scattering strongly depends on cloud altitude, cloud microphysics, and cloud overlap, which cannot be quantified analytically. Therefore, we focus on the clear-sky shortwave water vapor feedback, which we will refer to as λ_{SW} in the following.

Although shortwave water vapor absorption is well established to increase with warming[12], it is not obvious how exactly this leads to the numerical estimates of λ_{SW} from comprehensive climate models[9–11]. Furthermore, in contrast to the longwave feedback [e.g., refs. 5,13–15], little is known about the surface temperature dependence of λ_{SW} and what processes control it[16]. To address these questions, we build a hierarchy of analytical and numerical models for λ_{SW}, ranging from strongly idealized approximations to explicit radiative transfer simulations. In this way, we isolate the effects of different physical processes controlling λ_{SW}. This approach is inspired by recently developed analytical models for the clear-sky CO_2 radiative forcing and the clear-sky longwave feedback[5,6,17,18]. These models have helped bridge the gap between complex climate models and physical process understanding and thus have solidified our understanding of these important quantities.

In the following, we introduce a hierarchy of simple models for λ_{SW} and use it to study its magnitude and its dependence on surface temperature. In particular, we focus on the effect of different assumptions about water vapor absorption. In our most realistic model, in the following referred to as the

[1]Center for Earth System Research and Sustainability (CEN), Meteorological Institute, Universität Hamburg, Hamburg, Germany. [2]Department of Physics, University of Buea, Buea, Cameroon. [3]Present address: Institute for Atmospheric and Climate Science, ETH Zürich, Zurich, Switzerland.
✉e-mail: florian.roemer@env.ethz.ch

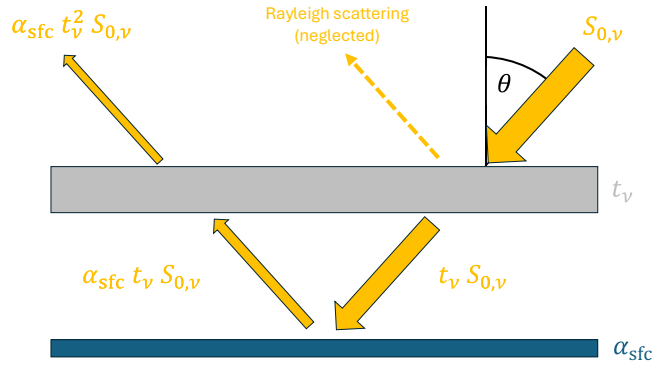

Fig. 1 | Sketch of single-layer model for the clear-sky shortwave water vapor feedback λ_{SW}. This model is used to derive a simple expression for the clear-sky upwelling shortwave radiation at the top of the atmosphere (in the absence of molecular Rayleigh scattering) based on incoming solar radiation $S_{0,\nu}$, solar incident angle θ, atmospheric transmissivity t_ν, and surface albedo α_{sfc}.

radiative transfer model, we use explicit radiative transfer simulations to assess the effects of processes not included in our analytical models. In this way, we provide insights into the underlying physical mechanisms that control λ_{SW}.

Results

A simple model for the clear-sky shortwave water vapor feedback

The shortwave water vapor feedback λ_{SW} quantifies how increasing water vapor absorption with warming reduces the amount of shortwave radiation that Earth reflects back into space ($F^{\uparrow}_{SW}$). In the clear-sky conditions studied here, this upwelling radiation comes from two different sources, namely reflection at Earth's surface and molecular Rayleigh scattering in Earth's atmosphere. However, while both contribute substantially to $F^{\uparrow}_{SW}$, molecular Rayleigh scattering is mostly independent of water vapor and thus does not strongly affect the water vapor feedback, as discussed in more detail below. Therefore, we represent the atmosphere by a non-scattering single layer.

To start, we recall that

$$\lambda_{SW} = \int_{\nu_0}^{\nu_1} \lambda_{SW,\nu}\, d\nu \tag{1}$$

where $\lambda_{SW,\nu}$ is the monochromatic feedback at a given wavenumber ν, and (ν_0, ν_1) refer to the lower and upper bound of the considered spectral range, respectively. In the following, we thus first derive our model for monochromatic radiation, that is, radiation of a single wavenumber. In this model, $F^{\uparrow}_{SW,\nu}$ is proportional to solar irradiance $S_{0,\nu}$, its incident zenith angle θ, and Earth's surface albedo α_{sfc}, as sketched in Fig. 1. Furthermore, $F^{\uparrow}_{SW,\nu}$ depends on the transmissivity of Earth's atmosphere to shortwave radiation t_ν. In our model, we approximate t_ν as a function of water vapor absorption only, neglecting absorption by other greenhouse gases and molecular scattering. Because solar radiation passes through Earth's atmosphere twice (before and after being reflected at the surface), $F^{\uparrow}_{SW,\nu}$ is proportional to t_ν^2 (Fig. 1). Therefore, we write the monochromatic clear-sky shortwave water vapor feedback as

$$\lambda_{SW,\nu} = -\frac{d}{dT} F^{\uparrow}_{SW,\nu} = -S_{0,\nu}\, \alpha_{sfc}\, \frac{d}{dT} t_\nu^2. \tag{2}$$

Here we assume that neither $S_{0,\nu}$ nor α_{sfc} vary with T in order to isolate $\lambda_{SW,\nu}$ from the surface albedo feedback. Furthermore, we neglect the spectral variations in α_{sfc} because these variations are very specific to the respective surface type. The atmospheric transmissivity can be expressed as

$$t_\nu = e^{-\tau_\nu}, \tag{3}$$

where τ_ν is the optical depth of Earth's atmosphere which we approximate as

$$\tau_\nu = \frac{\kappa_{H_2O,\nu}\, M_{H_2O}}{\cos(\theta)}, \tag{4}$$

$$M_{H_2O} = M_v^{ref}\, e^{-L/(R_v T)}. \qquad (\text{Clausius} - \text{Clapeyron relation}) \tag{5}$$

This approximation follows closely Jeevanjee[4], except for a few minor modifications described in the Methods section. In this model, τ_ν depends on two central quantities: First, the column water vapor $M_{H_2O}(T)$ based on the Clausius—Clapeyron relation in Eq. (5), and second, the mass absorption cross-section of water vapor $\kappa_{H_2O,\nu}$ which we assume to be independent of temperature. The parameters and physical constants in Eqs. (4) and (5) as well as their numerical values, can be found in the Methods section. Using Eqs. (3)–(5) and the chain rule, we can rewrite Eq. (2) as

$$\lambda_{SW,\nu} = 2\, S_{0,\nu}\, \alpha_{sfc}\, \frac{L}{R_v T^2}\, \tau_\nu\, e^{-2\tau_\nu}, \qquad (\text{monochromatic feedback}) \tag{6}$$

see "Methods" for a step-by-step derivation. Equation (6) reveals two interesting properties of $\lambda_{SW,\nu}$. First, while M_{H_2O} itself strongly increases with T, the relative increase in M_{H_2O} is proportional to $L/(R_v T^2)$. Because the change in atmospheric transmissivity—and thus $\lambda_{SW,\nu}$—depends on the relative change in M_{H_2O}, the Clausius-Clapeyron relation causes a negative dependence on T of $\lambda_{SW,\nu}$.

Second, $\lambda_{SW,\nu}$ is proportional to the product $\tau_\nu\, e^{-2\tau_\nu}$ —an expression that maximizes at $\tau_\nu = 0.5$ (black line in Fig. 2). In other words, our analytical model predicts that $\lambda_{SW,\nu}$ is strongest at wavenumbers where $\tau_\nu = 0.5$. This result holds remarkably well in the radiative transfer model when its normalized $\lambda_{SW,\nu}$ is binned with respect to the water-vapor optical depth (green line in Fig. 2, see "Methods" for details). This property is notable because several studies have shown that longwave emission and absorption maximize around $\tau_\nu = 1$ [e.g., refs. 18–21]. The main difference in our context is that, due to reflection at the surface, solar radiation passes through the atmosphere twice, doubling the atmospheric path length. We can further see that $\lambda_{SW,\nu}$ is substantial for a range of optical depth from about 0.05 to 2, corresponding to a transmissivity between around 0.95 and 0.14 (gray shading in Fig. 2). In the following, we will refer to this range as "transition region" because these τ_ν are located at the transition between the optically thin and optically thick regimes.

As mentioned above, the broadband λ_{SW} results from spectrally integrating the monochromatic feedback $\lambda_{SW,\nu}$ over a wide range of wavenumbers. Although we can simply perform this integration numerically, this misses a lot of interesting insights into the physical mechanisms that drive λ_{SW}. In particular, $\kappa_{H_2O,\nu}$ exhibits very complex spectral variations (see Fig. 3, thin purple line). In the following, we therefore present a hierarchy of simple models for λ_{SW} from the most idealized to the most realistic. The main difference between these models comes from different assumptions about the spectral variation of water vapor absorption $\kappa_{H_2O,\nu}$. For a better overview, the models are listed in Table 1.

Gray model

In our first and simplest model, we assume that both $\kappa_{H_2O,\nu}$ and $S_{0,\nu}$ are spectrally invariant ("gray"), that is, they do not vary with wavenumber ν. In this gray model, the spectral integral is represented by a single broadband value $\kappa^{gray}_{H_2O}$, resulting in a gray optical depth τ^{gray}. This gives

$$\lambda^{gray}_{SW} = 2\, S_0\, \alpha_{sfc}\, \frac{L}{R_v T^2}\, \tau^{gray}\, e^{-2\tau^{gray}}. \qquad (\text{gray model}) \tag{7}$$

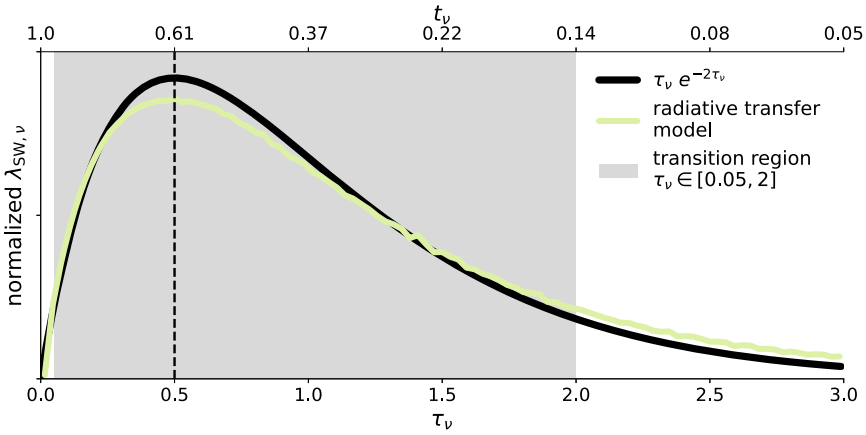

Fig. 2 | Monochromatic clear-sky shortwave water vapor feedback $\lambda_{SW,\nu}$ as function of water vapor optical depth τ_ν. Shown are the normalized $\lambda_{SW,\nu}$ for our analytical model (black) and the radiative transfer model (green), plotted against τ_ν (bottom axis) and transmissivity t_ν (top axis). The transition region where $\lambda_{SW,\nu}$ is strongest is shaded in gray. Details on the normalization procedure are provided in the Methods.

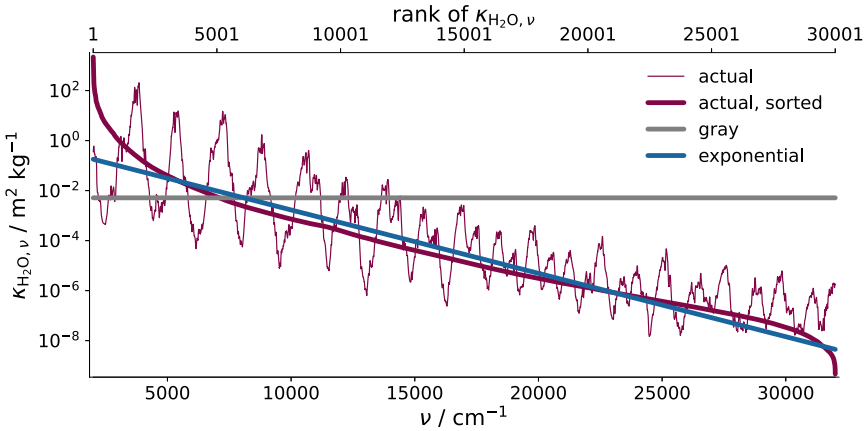

Fig. 3 | Mass absorption cross-section of water vapor $\kappa_{H_2O,\nu}$. Actual water vapor absorption spectrum, calculated for reference values of temperature T_κ = 280 K and pressure p_κ = 850 hPa (50 cm^{-1} moving average, thin purple line) and the same spectrum sorted by decreasing $\kappa_{H_2O,\nu}$ (thick purple line), as well as the exponential approximation of the sorted spectrum (blue), and our gray approximation (gray).

There is no canonical way to determine the value of $\kappa^{gray}_{H_2O}$. For the following analysis, we chose $\kappa^{gray}_{H_2O} \approx 5 \cdot 10^{-3}$ m^2 kg^{-1} which reproduces the insolation-weighted mean transmissivity at the global mean T = 290 K in our spectral model, visualized by the gray and purple lines in Fig. 4a (see "Methods" for details).

We evaluate the performance of the gray model in Fig. 4b (gray line). At 290 K, $\lambda^{gray}_{SW} \approx 0.6$ W m^{-2} K^{-1}, almost four times larger than the clear-sky estimate of 0.16 W m^{-2} K^{-1} of Soden et al.[9] (filled circle in Fig. 4b). Furthermore, λ^{gray}_{SW} exhibits a very pronounced dependence on T, with a peak of more than 0.8 W m^{-2} K^{-1} at around 300 K—in stark contrast to the much weaker dependence on T in the radiative transfer model (green line in Fig. 4b).

This discrepancy occurs because λ^{gray}_{SW} is sensitive to the value of τ^{gray} as stated by Eq. (7) and visualized in Fig. 2. Because M_{H_2O} increases by a factor of 40 between 270 K and 330 K, so does τ^{gray} and thus t^{gray} decreases from 0.96 to 0.16, passing through the entire transition region. However, the radiative transfer model shows a much weaker dependence on T; the insolation-weighted mean transmissivity in these simulations only decreases from 0.78 to 0.57 in the same range of T, as contrasted in Fig. 4a (gray and green lines, respectively).

This overestimation of the dependence on T is inherent in the gray model and occurs regardless of the value chosen for $\kappa^{gray}_{H_2O}$. This is because a higher value of $\kappa^{gray}_{H_2O}$ only shifts the peak in λ^{gray}_{SW} to lower values of M_{H_2O} — and thus lower T—and vice versa, but does not change the magnitude of the peak. Thus, the gray model is clearly not suited to capture the behavior of λ_{SW}.

Exponential model

In our second model, we include spectral variations in $\kappa_{H_2O,\nu}$. Instead of directly including the complex spectral dependency of $\kappa_{H_2O,\nu}$, we use an exponential approximation. This approach is motivated by the fact that when we resort the $\kappa_{H_2O,\nu}$ spectrum in decreasing order, the resulting $\kappa'_{H_2O,\nu}$ is largely well approximated by an exponential function, as demonstrated in Fig. 3. This approach also follows previous work in the longwave spectral range [e.g., refs. 4,5,22]. Due to the simple exponential dependency in the spectral dimension, the spectral integral λ^{exp}_{SW} can be expressed analytically as

$$\lambda^{exp}_{SW} = S_0\, \alpha_{sfc}\, \frac{L}{R_v T^2}\, \frac{l}{\Delta\nu} \left[e^{-2\tau^{exp}_{\nu}(\nu_1)} - e^{-2\tau^{exp}_{\nu}(\nu_0)} \right], \qquad \text{(exponential model)} \tag{8}$$

where $\Delta\nu = \nu_1 - \nu_0$ and l = 1713 cm^{-1} is the inverse slope of $\log(\kappa'_{H_2O,\nu})$, as described in more detail the "Methods".

The importance of considering the spectral dimension to capture λ^{exp}_{SW} is demonstrated in Fig. 5 which visualizes the spectral distributions of τ_ν, t_ν, and $\lambda_{SW,\nu}$. For better visibility, the spectra are sorted by descending $\kappa_{H_2O,\nu}$. Because $\kappa^{exp}_{H_2O,\nu}$ varies by many orders of magnitude throughout the spectrum, τ^{exp}_ν and thus t^{exp}_ν only lie within the transition region (gray shading) in a small part of the spectrum (thick solid lines in Fig. 5a, b). As a consequence, the integrated transmissivity in the exponential model only decreases from 0.94 to 0.74 between 270 K and 330 K (Fig. 4a, blue line). Although these absolute values of transmissivity are much higher than in the radiative transfer model, their change with T—the relevant quantity for λ_{SW}—is quite similar.

Furthermore, Fig. 5c demonstrates that indeed only the transition region exhibits substantial $\lambda^{exp}_{SW,\nu}$ (thick solid lines). This is why the integrated λ^{exp}_{SW} is much smaller than λ^{gray}_{SW} and much closer in magnitude to the radiative transfer model (Fig. 4b). As T increases, the spectral location of the transition region shifts, but its width does not change for most T, because it is

Table 1 | The model hierarchy used to study the clear-sky shortwave water vapor feedback λ_{SW}

Model	assumptions	included processes	equation
Gray model	$\kappa_{H_2O}^{gray}$ spectrally invariant	linear H_2O absorption	Eq. (7)
	S_0 spectrally invariant		
	α_{sfc} spectrally invariant		
	M_{H_2O} calculated from Eq. (5)		
Exponential model	$\kappa_{H_2O,\nu}^{exp}$ exponentially decreasing	linear H_2O absorption	Eq. (8)
	S_0 spectrally invariant		
	α_{sfc} spectrally invariant		
	M_{H_2O} calculated from Eq. (5)		
Spectral model	$\kappa_{H_2O,\nu}$ spectrum	linear H_2O absorption	Eq. (12)
	$S_{0,\nu}$ spectrum		
	α_{sfc} spectrally invariant		
	M_{H_2O} calculated from Eq. (5)		
Radiative transfer model	$\kappa_{H_2O,\nu}$ spectrum	linear H_2O absorption	–
	$S_{0,\nu}$ spectrum	non-linear H_2O absorption	
	α_{sfc} spectrally invariant	other greenhouse gases	
	M_{H_2O} from single-column model	molecular scattering	

primarily determined by the exponential fit parameter l in Eq. (8). This is why λ_{SW}^{exp} exhibits a much weaker dependence on T than λ_{SW}^{gray}, with a moderate increase to $\lambda_{SW}^{exp} = 0.2\ W\ m^{-2}\ K^{-1}$ at 270 K and a slow decrease at higher T (Fig. 4b, c).

The reasons for this dependence on T can be best understood by a closer inspection of Eq. (8), which contains two multiplicative terms that depend on T. The first term is the Clausius-Clapeyron factor $CC \equiv L/(R_v T^2)$ which induces a negative dependence on T as discussed above. The second T-dependent term of Eq. (8) is the factor

$$TR \equiv e^{-2\tau_\nu^{exp}(\nu_1)} - e^{-2\tau_\nu^{exp}(\nu_0)} = \max\left(t_\nu^{exp}\right)^2 - \min\left(t_\nu^{exp}\right)^2. \quad (9)$$

We refer to this factor as the transmittivity range factor (TR) because it quantifies the range between the maximum and minimum values of the squared transmissivities across the spectrum at a given T. For all T considered here, $\max(t_\nu^{exp})^2 \to 1$ due to the small $\kappa_{H_2O,\nu}$ at high ν. At $T \gtrsim 275$ K, $\min(t_\nu^{exp})^2 \to 0$ and thus $TR \to 1$. However, at $T \lesssim 275$ K, $\min(t_\nu^{exp})^2 > 0$ and thus $TR < 1$. This is visualized by the thick solid blue line in Fig. 5b that does not fall below around $t_\nu^{exp} \approx 0.75$ at the y-intercept. We can also think of this factor as quantifying the number of wavenumbers within the transition region. At low T, even the strongest absorbing parts of the spectrum are located far below the upper end of the transition region, and thus, parts of the transition region are not "occupied" by any wavenumber. This is visualized by the thick solid blue line in Fig. 5a that does not cover the entire transition range.

The analytic nature of Eq. (8) allows us to disentangle these two effects quantitatively. When we only consider the Clausius-Clapeyron effect, we set $TR = 1$ and the exponential model simplifies to

$$\lambda_{SW}^{exp,CC} = S_0\,\alpha_{sfc}\,\frac{L}{R_v T^2}\,\frac{l}{\Delta\nu}. \quad (\text{exponential model, CC only}) \quad (10)$$

As expected, $\lambda_{SW}^{exp,CC}$ continuously decreases with T (dotted blue line in Fig. 4c).

In contrast, we extract the effect of the transmissivity range on λ_{SW} by replacing T in the Clausius-Clapeyron factor by a constant reference value $T_{ref} = 290$ K:

$$\lambda_{SW}^{exp,TR} = S_0\,\alpha_{sfc}\,\frac{L}{R_v T_{ref}^2}\,\frac{l}{\Delta\nu}\left[e^{-2\tau_\nu^{exp}(\nu_1)} - e^{-2\tau_\nu^{exp}(\nu_0)}\right]. \quad (\text{exponential model, TR only}) \quad (11)$$

As expected, $\lambda_{SW}^{exp,TR}$ increases for $T \lesssim 275$ K and is constant at higher T (dashed blue line in Fig. 4c).

In this way, we can now understand the dependence on T of λ_{SW}^{exp}: Below 275 K, λ_{SW}^{exp} increases with T because the fraction of the spectrum within the transition region increases; at higher T this effect saturates, and thus the negative dependence on T of the Clausius-Clapeyron relation dominates. However, this dependence on T still differs substantially from the radiative transfer model, which exhibits a monotonously increasing λ_{SW} (solid blue and green lines in Fig. 4c, respectively).

Spectral model

In our third model, we replace the exponential $\kappa_{H_2O,\nu}^{exp}$ by the actual absorption spectrum $\kappa_{H_2O,\nu}$, and we also consider spectral variations in the incoming solar radiation $S_{0,\nu}$. This requires a numerical integration to calculate the broadband feedback as

$$\lambda_{SW}^{spec} = 2\,\alpha_{sfc}\,\frac{L}{R_v T^2}\int_{\nu_0}^{\nu_1} S_{0,\nu}\,\tau_\nu\,e^{-2\tau_\nu}\,d\nu. \quad (\text{spectral model}) \quad (12)$$

In contrast to the more idealized gray and exponential models, this semi-analytical spectral model reproduces the continuously increasing λ_{SW} seen in the radiative transfer model, although it still underestimates the magnitude of the increase (purple line in Fig. 4c). This better performance of the spectral model is not caused by the inclusion of the solar spectrum. This is because the sawtooth-like shape of $\kappa_{H_2O,\nu}$ means that both relatively high and relatively low values of $\kappa_{H_2O,\nu}$ — and thus τ_ν—are distributed across the solar spectrum, thus canceling out most systematic effects of spectral variations in the solar irradiance (not shown). This further indicates that spectral variations in α_{sfc}, which we neglect in this study, presumably also have a negligible effect on λ_{SW}.

Instead, the main reason for the better performance of the spectral model compared to the exponential model originates from details of water vapor spectroscopy. This can be readily seen in Fig. 5 which compares the spectral distributions of τ_ν and $\lambda_{SW,\nu}$ between the exponential and the spectral model (thick solid and dotted lines in panels a and c, respectively). In the exponential model, the slope of $\log(\tau_\nu)$ is constant by definition and thus the width of the spectral region that has τ_ν within the transition region stays constant above around 275 K, as described in the previous section. In contrast, the actual τ_ν used in the spectral model features a much steeper slope for the highest values of $\kappa_{H_2O,\nu}$, which correspond to comparatively few strong water vapor absorption lines (dotted lines in Fig. 5a). At low T— and thus small M_{H_2O} — it is only these few strong absorption lines with large $\kappa_{H_2O,\nu}$ that produce values of τ_ν within the transition region. This is visualized by the blue dotted line that transects the gray-shaded transition region at a quite steep slope (Fig. 5a). At higher T, a much larger number of intermediate $\kappa_{H_2O,\nu}$ produce values of τ_ν within the transition region. This is visualized by the yellow dotted line that transects the gray-shaded transition region at a much flatter slope (Fig. 5a). As a consequence, the width of the spectral region that contributes to λ_{SW}—and thus λ_{SW} itself— continuously increases with T in the spectral model, as demonstrated in Fig. 5c (dotted

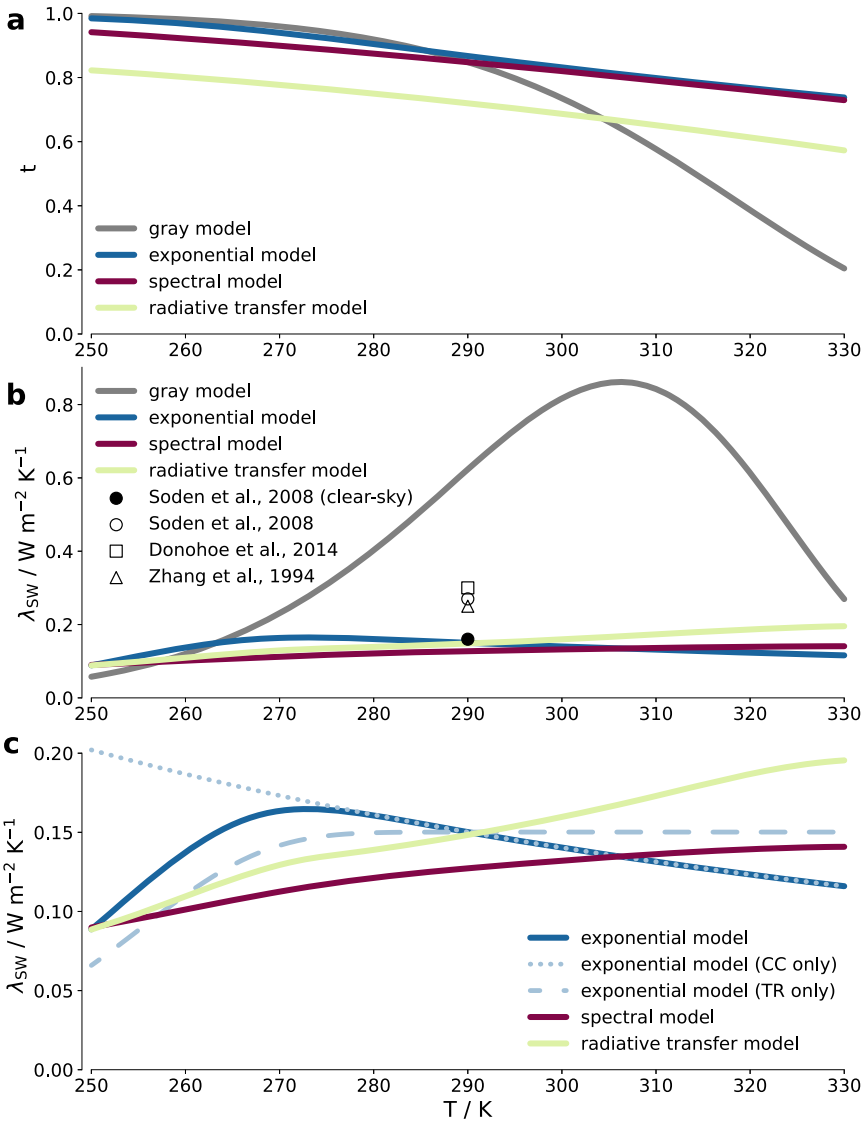

Fig. 4 | Comparison of different models for the clear-sky shortwave water vapor feedback λ_{SW}. Dependence of (**a**) atmospheric transmissivity and (b,c) clear-sky shortwave water vapor feedback λ_{SW} on surface temperature T in our model hierarchy. For reference, previous estimates of the global mean clear-sky and all-sky λ_{SW} are shown in (**b**). In (**c**), we disentangle the effects of the Clausius-Clapeyron factor (CC) and the transmissivity range factor (TR) on λ_{SW}.

lines). At the T considered here, this effect is stronger than the negative dependence on T induced by the Clausius-Clapeyron factor, which explains the positive dependence on T of λ_{SW}^{spec}.

Even for the spectral model, the spectral distributions of τ_ν and t_ν differ quite substantially from the radiative transfer model (Fig. 5a, b). This is because of the approximation that τ_ν is governed only by water vapor absorption. In reality, τ_ν is also shaped, among other factors, by absorption of other greenhouse gases and molecular scattering, as discussed in more detail in the following section. However, most of these other factors do not vary with T and therefore their inclusion has a much weaker effect on $\lambda_{SW,\nu}$ (Fig. 5c).

Radiative transfer model

Our final and most realistic model is not based on Eqs. (4)–(6) but instead consists of explicit radiative transfer simulations based on the line-by-line model ARTS[23,24]. In contrast to the idealized models above, we do not derive M_{H_2O} from Eq. (5) but instead use atmospheric profiles of temperature and water vapor concentration based on the single-column atmospheric model konrad[25–27] (see "Methods" for details). Hence, this model includes processes not captured by the more idealized models presented above, such as deviations from the linear relationship between M_{H_2O} and τ_ν assumed in Eq. (4), absorption by other greenhouse gases, and molecular Rayleigh scattering (see Table 1).

As mentioned above, both the magnitude and dependence on T of λ_{SW} are similar between the spectral model and the radiative transfer model. However, the radiative transfer model generally exhibits higher values of λ_{SW}, particularly at high T. These differences can be attributed to deviations from some of our approximations. We disentangle the effects of these approximations by analyzing different configurations of both the spectral model and the radiative transfer model in which we successively remove discrepancies between the two models. The different steps are described below and visualized in Fig. 6a.

The calculation of M_{H_2O} in Eq. (5) makes two major approximations that cause it to underestimate the increase of M_{H_2O} with warming compared to konrad (solid purple and green lines in Fig. 6b, respectively). First, equation (5) only considers the equilibrium water vapor pressure e_s over water, while konrad accounts for the lower e_s over ice[26]. When we analogously calculate e_s over water in konrad, the discrepancies decrease below around 290 K (dashed green line in Fig. 6b). Second, Eq. (5) applies the Clausius-Clapeyron scaling of M_{H_2O} to surface temperature T_s rather than the temperature of the lower troposphere T_{LT} where most water vapor is located. This part of the atmosphere is somewhat colder than the surface, but warms at a similar rate as T increases. To approximate this behavior in our spectral model, we replace T in Eqs. (5) and (12) by $T_{LT} = T - 16$ K; this empirical tuning yields a much better agreement with konrad (dashed purple line in Fig. 6b). The combined inclusion of these two effects

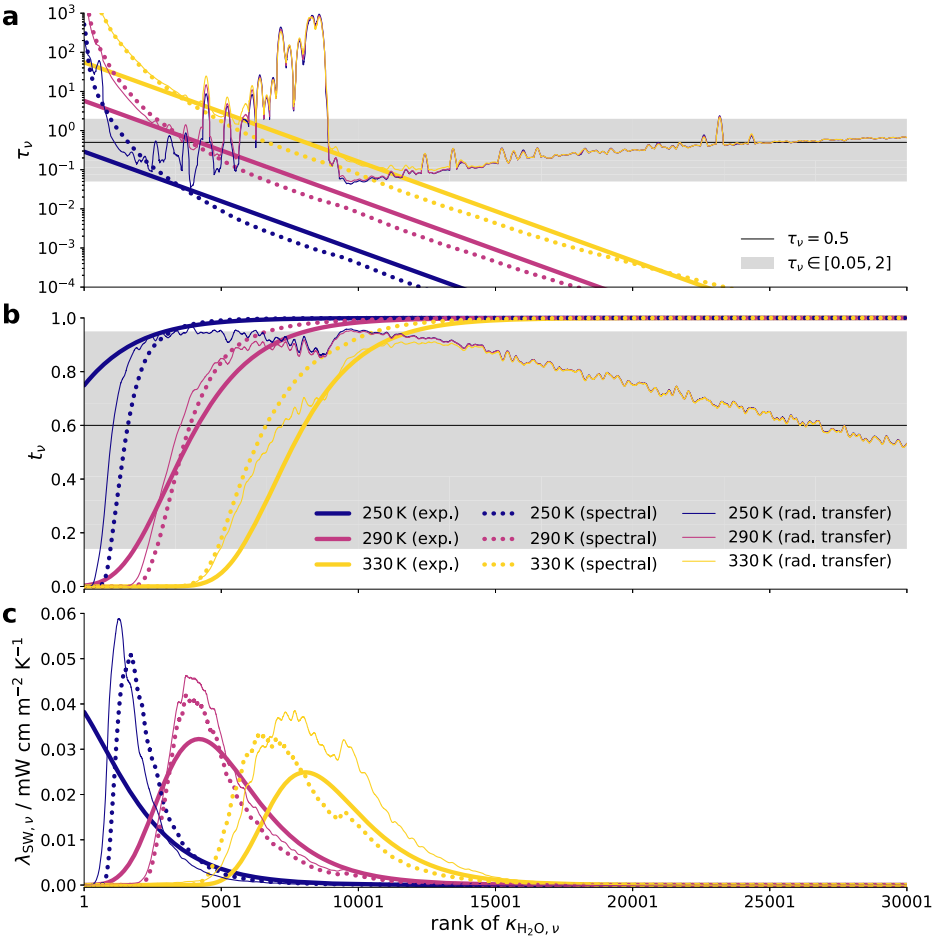

Fig. 5 | Monochromatic optical depth τ_ν, transmissivity t_ν, and clear-sky shortwave water vapor feedback $\lambda_{SW,\nu}$. Spectral distributions of (**a**) τ_ν, (**b**) t_ν, and (**c**) $\lambda_{SW,\nu}$ for different surface temperatures T, all sorted by descending $\kappa_{H_2O,\nu}$. In (**a**) and (**b**), the transition region is shaded in gray. Shown are the curves for the exponential model (thick solid lines), the spectral model (thick dotted lines), and the radiative transfer model (thin solid lines).

substantially decreases the discrepancies in λ_{SW} (dashed light green and dashed purple lines in Fig. 6a).

In our analytical models, we neglect Rayleigh scattering by air molecules, which is responsible for ≈ 30 % of $F^{\uparrow}_{SW}$. This is why even the spectral model strongly underestimates τ_ν (and overestimates t_ν) at ranks of $\kappa_{H_2O,\nu}$ above 10,000, the spectral region where Rayleigh scattering is stronger than water vapor absorption (Fig. 5a,b). However, a large part of the scattering occurs above the atmospheric boundary layer where most water vapor is located. Furthermore, water vapor absorption tends to be strongest for low wavenumbers ν, whereas Rayleigh scattering mostly occurs at high ν. Therefore, radiation scattered by air molecules is much less likely to be absorbed by water vapor compared with radiation reflected at the surface, and thus is much less affected by the increase in M_{H_2O} with warming. Therefore, the λ_{SW} in our radiative transfer model only decreases slightly when we perform simulations without scattering (dashed medium green line in Fig. 6a).

In our analytical models, we also neglect the absorption of greenhouse gases other than water vapor, such as CO_2, CH_4, and O_3. This absorption reduces the effect of water vapor by causing some wavenumbers to be optically thick regardless of water vapor concentration, effectively "masking" water vapor absorption, and thus reducing the number of wavenumbers that pass through the transition region. This effect is particularly striking when comparing the spectra of τ_ν between the spectral model and the radiative transfer model for the ranks of $\kappa_{H_2O,\nu}$ between 2500 and 10000 (Fig. 5a). This part of the spectrum largely consists of wavenumbers located in windows between strong water vapor absorption bands but close to the band centers of other greenhouse gases (not shown). Therefore, the radiative transfer model exhibits very high values of τ_ν despite relatively moderate values of $\kappa_{H_2O,\nu}$ in these spectral regions, which by construction are not captured by the spectral model. However, because the absorption by non-H_2O greenhouse gases does not strongly depend on T, this has only a weak effect on λ_{SW}: When we remove all greenhouse gases other than water vapor from our radiative transfer model, λ_{SW} only increases slightly (short-dashed dark green line in Fig. 6a).

Another simplification in our analytical models is the assumption that τ_ν scales linearly with M_{H_2O}. Although this is a decent approximation at low T, water vapor absorption scales supralinearly with T, causing a stronger λ_{SW} at high T. This supralinear scaling is caused by self-broadening mechanisms by which interactions between water molecules increase the width of their absorption lines [e.g., ref. 28]. Part of this broadening is described by the water vapor self continuum, which scales quadratically with water vapor concentration [e.g., ref. 29]. When we run the radiative transfer model without water vapor continuum absorption, that is, only including water vapor line absorption, the resulting λ_{SW} is in good agreement with our spectral model below around 310 K; however, the spectral model slightly overestimates λ_{SW} below 290 K and underestimates it above 290 K (dotted black and dashed purple lines in Fig. 6a, respectively). This is presumably because water vapor line absorption is also subject to self-broadening mechanisms and thus also increases supralinearly with M_{H_2O}.

Finally, in our analytical models, we also neglect the temperature dependencies of two quantities used to calculate M_{H_2O}. First, we neglect the temperature dependence of the reference water vapor column M_v^{ref}, which in the model of Jeevanjee[4] changes by approximately 0.2 % K^{-1}. Second, we neglect the temperature dependence of the latent heat of vaporization for H_2O, L, which decreases with T by around −0.1 % K^{-1} [e.g., ref. 30]. However, since the temperature dependence of M_{H_2O} is dominated by the Clausius-Clapeyron factor $L/(R_v T^2) \approx 7$ % K^{-1}, both of these approximations presumably have only a minor effect.

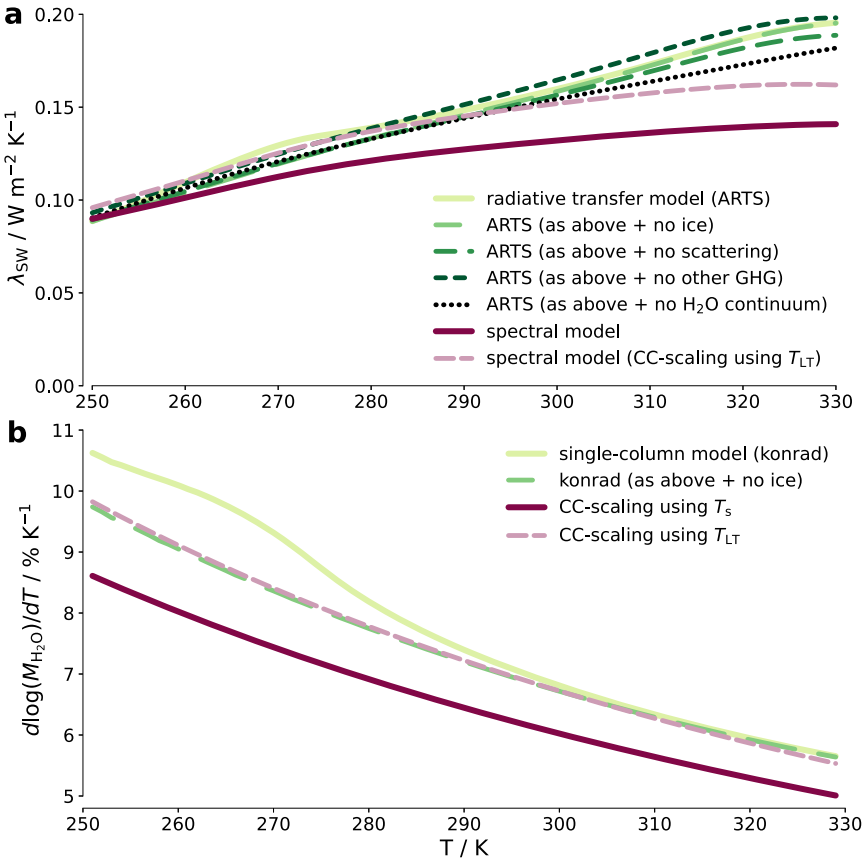

Fig. 6 | Effect of clear-sky processes not included in our analytical models. a Comparison between λ_{SW} from different versions of the spectral model (purple) and radiative transfer model (green). **b** Relative change in water vapor column M_{H_2O} with warming based on the simple Clausius-Clapeyron (CC) scaling in Eq. (5) (purple) and based on the single-column model konrad on which our radiative transfer model is based (green).

Discussion

We present a model hierarchy ranging from analytical models to radiative transfer simulations and use these models to study the clear-sky shortwave water vapor feedback λ_{SW}. In our analytical models, λ_{SW} is proportional to the change in the square of atmospheric transmissivity t_ν with temperature T. This means that λ_{SW} originates mainly from spectral regions that transition from optically thin to optically thick, peaking at an optical depth of $\tau_\nu = 0.5$. In this way λ_{SW} departs from the $\tau_\nu = 1$ "law" previously found for longwave emission [e.g., refs. 18–21].

Furthermore, we highlight the role of water vapor spectroscopy in determining both the magnitude and temperature dependence of λ_{SW}. Because water vapor absorption $\kappa_{H_2O,\nu}$ varies across many orders of magnitude throughout the shortwave spectrum, only a small part of the spectrum contributes to λ_{SW} at any given temperature. This behavior is overall well captured by approximating $\kappa_{H_2O,\nu}$ to decrease exponentially with wavenumber ν. However, the dependence of λ_{SW} on surface temperature T is determined by subtleties in the spectrum of $\kappa_{H_2O,\nu}$ that cause the fraction of the spectrum with $\tau_\nu \approx 0.5$ to continuously increase with temperature. This demonstrates that the spectral dimension is a useful perspective not only for the longwave [e.g., refs. 3,13,31,32], but also for the shortwave part of Earth's radiative feedback.

At global mean $T = 290$ K, most of our models yield a λ_{SW} between 0.13 W m^{-2} K^{-1} and 0.15 W m^{-2} K^{-1}, similar to the estimate of Soden et al.[9] of 0.16 W m^{-2} K^{-1}, albeit slightly smaller. As mentioned above, the all-sky λ_{SW} is substantially stronger due to the effect of scattering by clouds and aerosols. Although these effects cannot be quantified analytically, it would be interesting to systematically assess the effects of cloud altitude, cloud microphysics, and cloud overlap on the magnitude of λ_{SW}.

With this work, we provide simple physical explanations for the magnitude of λ_{SW} and its dependence on T, complementing similar studies of the longwave feedback[3–6]. In this way, we provide a more complete picture of the role of water vapor in Earth's climate system, bridging the gap between complex climate models and theoretical process understanding.

Methods

Monochromatic feedback

From Eq. (2), we use Eqs. (3)–(5) and the chain rule to derive Eq. (6) as follows:

$$\begin{aligned}\lambda_{SW,\nu} &= -S_{0,\nu}\,\alpha_{sfc}\,\tfrac{d}{dT}\left(t_\nu^2\right)\\ &= -S_{0,\nu}\,\alpha_{sfc}\,\tfrac{d}{dT}\left(e^{-2\tau_\nu}\right)\\ &= 2\,S_{0,\nu}\,\alpha_{sfc}\,\tfrac{d\tau_\nu}{dT}\,e^{-2\tau_\nu}\\ &= 2\,S_{0,\nu}\,\alpha_{sfc}\,\tfrac{d\log(\tau_\nu)}{dT}\,\tau_\nu\,e^{-2\tau_\nu}\\ &= 2\,S_{0,\nu}\,\alpha_{sfc}\,\tfrac{L}{R_v\,T^2}\,\tau_\nu\,e^{-2\tau_\nu}. \qquad \text{(monochromatic feedback)}\end{aligned} \tag{13}$$

To compare the behavior of this simple analytical model with the radiative transfer model in Fig. 2, a normalization is performed. For the analytical model, this simply means isolating the mathematical expression $\tau_\nu\,e^{-2\tau_\nu}$ and plotting it as a function of τ_ν (black line). For the radiative transfer model, we bin its full $\lambda_{SW,\nu}$ with respect to the optical depth τ_ν of water vapor absorption in the interval $\tau_\nu \in [0, 3]$ in steps of 0.01 and calculate the average $\lambda_{SW,\nu}$ over each bin. We then scale these averages so that their integral over the interval $\tau_\nu \in [0, 3]$ is equal to that of the analytical expression $\tau_\nu\,e^{-2\tau_\nu}$ to compare the variations with τ_ν (green line).

Gray model

We approximate the spectral integral by replacing the monochromatic τ_ν by a single value

$$\tau^{gray} = \frac{\kappa_{H_2O}^{gray}\,M_{H_2O}}{\cos(\theta)}. \tag{14}$$

To evaluate the model numerically, we chose $\kappa_{H_2O}^{gray}$ so that our gray model reproduces the insolation-weighted zenith transmissivity of Earth's atmosphere to shortwave radiation at the global mean surface temperature of T = 290 K, which we calculate using the actual spectra of $\kappa_{H_2O,\nu}$ and $S_{0,\nu}$. This gives

$$\begin{aligned}\kappa_{H_2O}^{gray} &= -\frac{\cos(\theta)}{M_{H_2O}(290\,\mathrm{K})}\log\left(\frac{1}{S_0}\int_{\nu_0}^{\nu_1} S_{0,\nu}\, e^{-\kappa_{H_2O,\nu} M_{H_2O}(290\mathrm{K})/\cos(\theta)}\, d\nu\right)\\ &= -\frac{\cos(48.19^\circ)}{21.4\,\mathrm{kg\,m^{-2}}}\log(0.85)\\ &= 5.1\cdot 10^{-3}\,\mathrm{m^2\,kg^{-1}}.\end{aligned} \tag{15}$$

Exponential model

We account for spectral variations in τ_ν but not in $S_{0,\nu}$, yielding the monochromatic

$$\lambda_{SW,\nu}^{exp} = 2\,\frac{S_0}{\Delta\nu}\,\alpha_{sfc}\,\frac{L}{R_v T^2}\,\tau_\nu^{exp} e^{-2\tau_\nu^{exp}}, \qquad \text{(exponential model, monochromatic)} \tag{16}$$

from which we infer the broadband exponential feedback by spectral integration:

$$\lambda_{SW}^{exp} = 2\,\frac{S_0}{\Delta\nu}\,\alpha_{sfc}\,\frac{L}{R_v T^2}\int_{\nu_0}^{\nu_1}\tau_\nu^{exp}\, e^{-2\tau_\nu^{exp}}\, d\nu. \tag{17}$$

This integral can be expressed analytically using the exponential ansatz

$$\tau_\nu^{exp} = \frac{M_{H_2O}}{\cos\theta}\,\kappa_{H_2O,\nu}^{exp} = \frac{M_{H_2O}}{\cos\theta}\,\kappa_0\, e^{-\nu/l}. \tag{18}$$

and thus

$$\frac{d\log(\tau_\nu^{exp})}{d\nu} = \frac{d\log\left(\kappa_{H_2O,\nu}^{exp}\right)}{d\nu} = -\frac{1}{l}, \tag{19}$$

similar to Jeevanjee et al.[18] and Jeevanjee & Fueglistaler[21]. We thus rewrite Eq. (17) as

$$\begin{aligned}\lambda_{SW}^{exp} &= 2\,S_0\,\alpha_{sfc}\,\tfrac{L}{R_v T^2}\,\tfrac{1}{\Delta\nu}\int_{\nu_0}^{\nu_1}(-l)\,\tfrac{d\log(\tau_\nu)}{d\nu}\,\tau_\nu^{exp} e^{-2\tau_\nu^{exp}}\, d\nu\\ &= S_0\,\alpha_{sfc}\,\tfrac{L}{R_v T^2}\,\tfrac{l}{\Delta\nu}\int_{\nu_0}^{\nu_1}\tfrac{d}{d\nu}e^{-2\tau_\nu^{exp}}\, d\nu\\ &= S_0\,\alpha_{sfc}\,\tfrac{L}{R_v T^2}\,\tfrac{l}{\Delta\nu}\left[e^{-2\tau_\nu^{exp}(\nu_1)} - e^{-2\tau_\nu^{exp}(\nu_0)}\right]. \qquad \text{(exponential model)}\end{aligned} \tag{20}$$

To evaluate the model numerically, we first resort $\kappa_{H_2O,\nu}$ in decreasing order, similar to the approach of Romps et al.[22]. We then perform a linear least-squares fit against the resorted $\log(\kappa'_{H_2O,\nu})$ as a function of wavenumber ν. This gives us the exponential fit

$$\kappa_{H_2O,\nu}^{exp} = 0.57\,\mathrm{m^2\,kg^{-1}}\cdot e^{-\nu/1713\,\mathrm{cm^{-1}}}. \tag{21}$$

Spectral model

We include the actual spectra of both τ_ν and $S_{0,\nu}$ which yields

$$\lambda_{SW,\nu}^{spec} = 2\,\alpha_{sfc}\,\frac{L}{R_v T^2}\,S_{0,\nu}\,\tau_\nu e^{-2\tau_\nu}. \qquad \text{(spectral model, monochromatic)} \tag{22}$$

Due to the complex spectral dependencies of τ_ν and $S_{0,\nu}$, the broadband feedback has to be inferred by evaluating the integral numerically:

$$\lambda_{SW}^{spec} = 2\,\alpha_{sfc}\,\frac{L}{R_v T^2}\int_{\nu_0}^{\nu_1} S_{0,\nu}\,\tau_\nu e^{-2\tau_\nu}\, d\nu. \qquad \text{(spectral model)} \tag{23}$$

Radiative transfer model

For our radiative transfer simulations, we use the line-by-line model ARTS version 2.6[23,24], which was recently extended to support radiation from a solar source[33]. We cover a spectral range of 2000–32000 cm^{-1} with a spectral resolution of 1 cm^{-1}, disabling thermal emission. We include absorption by H_2O, CO_2, O_3, CH_4, N_2, and O_2. Line absorption is calculated using the internal ARTS Catalog Data, which in turn is based on the high-resolution transmission molecular absorption database [HITRAN,[34]] as of 2022-05-02. Continuum absorption is calculated using the MT_CKD models for CO_2 and N_2 (both version 2.5), O_2 (version 1.0), and water vapor (version 4.0)[35]. For computational efficiency, we use the ARTS-internal absorption lookup table[36].

The atmospheric input is from the single-column model konrad version 1.0.1[25–27] and emulates the properties of our analytical models: For a given surface temperature T between 250 K and 330 K, we assume a constant temperature lapse rate Γ = 6.5 K km^{-1} in the troposphere until T_{strat} = 194 K is reached; in the stratosphere above we assume constant $T = T_{strat}$. Relative humidity is set to 75 % in the troposphere, in the stratosphere we use the same water vapor volume mixing ratio as at the tropopause. We use 128 vertical atmospheric layers; surface albedo, solar zenith angle, and solar irradiance are the same as in our analytical models (see below). The trace gas concentrations for CO_2, CH_4, and O_3 follow Wing et al.[37].

Parameter selection

Our analytical models contain a number of parameters, which we chose based on several previous studies (see Table 2). The model is very similar to the model developed by Jeevanjee[4], but differs in a few details. First, we scale the optical depth τ_ν by a factor of $1/\cos(\theta)$ to account for the fact that the solar radiation is incident at an angle θ relative to the zenith[37,38]; see below for a discussion of how we chose θ. Second, instead of the pressure scaling term used by Jeevanjee[4], we approximate the effect of pressure broadening by calculating the water vapor mass absorption cross-section $\kappa_{H_2O,\nu}$ at an effective reference temperature and pressure, following Stevens & Kluft[6]. Furthermore, we use different reference temperature values to derive the

Table 2 | Parameters and physical constants used in our models

	Meaning	Value	Reference
α_{sfc}	Surface albedo	0.12	L'Ecuyer et al.[39]
S_0	Insolation	340 W m^{-2}	Cronin[38]
θ	Solar zenith angle	48.19°	Cronin[38]
T_κ	Temperature for calculation of $\kappa_{H_2O,\nu}$	280 K	Stevens & Kluft[6]
p_κ	Pressure for calculation of $\kappa_{H_2O,\nu}$	850 hPa	Stevens & Kluft[6]
T_{strat}	Stratospheric temperature	194 K	Stevens & Kluft[6]
T_s	Reference surface temperature	290 K	
$\mathcal{R}$	Relative humidity	0.75	Jeevanjee[4]
Γ	Temperature lapse rate	6.5 K km^{-1}	Jeevanjee[4]
p_v^{ref}	Reference water vapor pressure	$2.5\cdot 10^{11}$ Pa	Jeevanjee[4]
ν_0	Lower bound of spectral range	2000 cm^{-1}	
ν_1	Upper bound of spectral range	32000 cm^{-1}	
L	Latent heat of vaporization for H_2O	$2.5\cdot 10^6$ J kg^{-1}	
R_v	Specific gas constant of water vapor	461.5 J kg^{-1} K^{-1}	

constant

$$M_{\mathrm{v}}^{\mathrm{ref}} = \frac{\mathcal{R}\, p_{\mathrm{v}}^{\mathrm{ref}}\,(T_{\mathrm{s}} + T_{\mathrm{strat}})}{2\Gamma L}. \tag{24}$$

Following Stevens & Kluft[6], we use a stratospheric temperature of T_{strat} = 194 K instead of 210 K, but λ_{SW} is not very sensitive to this choice. We use a fixed surface temperature of T_{s} = 290 K instead of the variable $T \in$ [250 K, 330 K], which would induce a weak temperature dependence in $M_{\mathrm{v}}^{\mathrm{ref}}$. This makes the model conceptually simpler and only has a minor impact (see above).

Our analytical models state that λ_{SW} scales directly with surface albedo α_{sfc}, consistent with the previous finding that λ_{SW} is strongest in the polar regions, where the surface albedo is highest[9]. This in turn means that quantitative assessments of λ_{SW} are very sensitive to the choice of α_{sfc}. The surface albedo $\alpha_{\mathrm{sfc}} = 0.12$ in our model represents the global mean clear-sky albedo, which we derive from the global mean ratio of reflected shortwave radiation (USW) and downwelling shortwave radiation (DSR) at the surface [[39], their Tab. 4].

In our model, we neglect variations in the solar zenith angle, which in the real world differs between the polar regions and the tropics, but instead only consider one single incident angle $\theta = 48.19^{\circ}$. This angle represents the global mean insolation-weighted zenith angle and, combined with a solar constant of $S_0^* = 510\ \mathrm{W\,m^{-2}}$ yields the global mean insolation of $S_0 = S_0^* \cos(\theta) = 340\ \mathrm{W\,m^{-2}}$, as described in detail by Cronin[38]. This means that our estimate at low T is presumably higher than the local λ_{SW} expected in Earth's polar regions, which in the real world exhibit lower solar irradiance and vice versa for tropical regions. The solar spectrum used for both the spectral model and the radiative transfer model is the *SSI CDR reference spectrum of May 2004*[40], rescaled to a solar constant of $S_0^* = 510\ \mathrm{W\,m^{-2}}$[37].

Data availability

The model output data used in this study can be found at Roemer et al.[41].

Code availability

The code used in this study can be found at Roemer et al.[42].

Received: 12 February 2025; Accepted: 19 June 2025;
Published online: 19 July 2025

References

1. Manabe, S. & Wetherald, R. T. Thermal equilibrium of the atmosphere with a given distribution of relative humidity. *J. Atmos. Sci.* **24**, 241–259 (1967).
2. Ingram, W. A very simple model for the water vapour feedback on climate change. *Q. J. R. Meteorol. Soc.* **136**, 30–40 (2010).
3. Jeevanjee, N., Koll, D. D. B. & Lutsko, N. "Simpson's Law" and the spectral cancellation of climate feedbacks. *Geophys. Res. Lett.* **48**, e2021GL093699 (2021).
4. Jeevanjee, N. Climate sensitivity from radiative-convective equilibrium: a chalkboard approach. *Am. J. Phys.* **91**, 731–745 (2023).
5. Koll, D. D. B., Jeevanjee, N. & Lutsko, N. J. An analytic model for the clear-sky longwave feedback. *J. Atmos. Sci.* **80**, 1923–1951 (2023).
6. Stevens, B. & Kluft, L. A colorful look at climate sensitivity. *Atmos. Chem. Phys.* **23**, 14673–14689 (2023).
7. Held, I. M. & Shell, K. M. Using relative humidity as a state variable in climate feedback analysis. *J. Clim.* **25**, 2578–2582 (2012).
8. Hogan, R. J. & Matricardi, M. Evaluating and improving the treatment of gases in radiation schemes: the Correlated K-Distribution Model Intercomparison Project (CKDMIP). *Geosci. Model Dev.* **13**, 6501–6521 (2020).
9. Soden, B. J. et al. Quantifying climate feedbacks using radiative kernels. *J. Clim.* **21**, 3504–3520 (2008).
10. Zhang, M. H., Hack, J. J., Kiehl, J. T. & Cess, R. D. Diagnostic study of climate feedback processes in atmospheric general circulation models. *J. Geophys. Res. Atmos.* **99**, 5525–5537 (1994).
11. Donohoe, A., Armour, K. C., Pendergrass, A. G. & Battisti, D. S. Shortwave and longwave radiative contributions to global warming under increasing CO_2. *Proc. Natl. Acad. Sci. USA* **111**, 16700–16705 (2014).
12. Ramanathan, V. & Coakley Jr, J. A. Climate modeling through radiative-convective models. *Rev. Geophys.* **16**, 465–489 (1978).
13. Koll, D. D. B. & Cronin, T. W. Earth's outgoing longwave radiation linear due to H_2O greenhouse effect. *Proc. Natl. Acad. Sci. USA* **115**, 10293–10298 (2018).
14. Kluft, L., Dacie, S., Brath, M., Buehler, S. A. & Stevens, B. Temperature-dependence of the clear-sky feedback in radiative-convective equilibrium. *Geophys. Res. Lett.* **48**, e2021–GL094649 (2021).
15. Seeley, J. T. & Jeevanjee, N. H_2O windows and CO_2 radiator fins: a clear-sky explanation for the peak in equilibrium climate sensitivity. *Geophys. Res. Lett.* **48**, e2020–GL089609 (2021).
16. Menang, K. P., Buehler, S. A., Kluft, L., Hogan, R. J. & Roemer, F. E. Variation in shortwave water vapour continuum and impact on clear-sky shortwave radiative feedback. *EGUsphere* 1–22 (2024).
17. Wilson, D. J. & Gea-Banacloche, J. Simple model to estimate the contribution of atmospheric CO_2 to the Earth's greenhouse effect. *Am. J. Phys.* **80**, 306–315 (2012).
18. Jeevanjee, N., Seeley, J. T., Paynter, D. & Fueglistaler, S. An analytical model for spatially varying clear-sky CO_2 forcing. *J. Clim.* **34**, 9463–9480 (2021).
19. Pierrehumbert, R. T. *Principles of Planetary Climate*. (Cambridge University Press, Cambridge, 2010).
20. Huang, Y. & Bani Shahabadi, M. Why logarithmic? A note on the dependence of radiative forcing on gas concentration. *J. Geophys. Res.: Atmos.* **119**, 13683–13689 (2014).
21. Jeevanjee, N. & Fueglistaler, S. Simple spectral models for atmospheric radiative cooling. *J. Atmos. Sci.* **77**, 479–497 (2020).
22. Romps, D. M., Seeley, J. T. & Edman, J. P. Why the forcing from carbon dioxide scales as the logarithm of its concentration. *J. Clim.* **35**, 4027–4047 (2022).
23. Buehler, S. A. et al. The atmospheric radiative transfer simulator ARTS, version 2.6—deep Python integration. *J. Quant. Spectrosc. Radiat. Transf.* **341**, 109443 (2025).
24. Eriksson, P., Buehler, S. A., Davis, C. P., Emde, C. & Lemke, O. ARTS, the atmospheric radiative transfer simulator, version 2. *J. Quant. Spectrosc. Radiat. Transf.* **112**, 1551–1558 (2011).
25. Kluft, L., Dacie, S. & Bourdin, S. *Atmtools/konrad: Fix ARTS and cloud interfaces*. Zenodo https://doi.org/10.5281/zenodo.6046423 (2022).
26. Kluft, L., Dacie, S., Buehler, S. A., Schmidt, H. & Stevens, B. Re-examining the first climate models: climate sensitivity of a modern radiative–convective equilibrium model. *J. Clim.* **32**, 8111–8125 (2019).
27. Dacie, S. et al. A 1D RCE study of factors affecting the tropical tropopause layer and surface climate. *J. Clim.* **32**, 6769–6782 (2019).
28. Clough, S. A., Kneizys, F. X. & Davies, R. W. Line shape and the water vapor continuum. *Atmos. Res.* **23**, 229–241 (1989).
29. Burch, D. E. & Alt, R. L.*Continuum Absorption by H_2O in the 700–1200 cm^{-1} and 2400–2800 cm^{-1} Windows*, Tech. Rep. (1984).
30. Henderson-Sellers, B. A new formula for latent heat of vaporization of water as a function of temperature. *Q. J. R. Meteorol. Soc.* **110**, 1186–1190 (1984).
31. Huang, X., Chen, X., Soden, B. J. & Liu, X. The spectral dimension of longwave feedback in the CMIP3 and CMIP5 experiments. *Geophys. Res. Lett.* **41**, 7830–7837 (2014).
32. Roemer, F. E., Buehler, S. A., Brath, M., Kluft, L. & John, V. O. Direct observation of Earth's spectral long-wave feedback parameter. *Nat. Geosci.* **16**, 416–421 (2023).

33. Brath, M., Petersen, J., Buehler, S. A. & Eriksson, P. *Extending the Atmospheric Radiative Transfer Simulator (Arts) to Shortwave Radiation.* (SSRN Scholarly Paper. 2024).
34. Gordon, I. E. et al. The HITRAN2020 molecular spectroscopic database. *J. Quant. Spectrosc. Radiat. Transf.* **277**, 107949 (2022).
35. Mlawer, E. J., Cady-Pereira, K. E., Mascio, J. & Gordon, I. E. The inclusion of the MT_ckd water vapor continuum model in the HITRAN molecular spectroscopic database. *J. Quant. Spectrosc. Radiat. Transf.* **306**, 108645 (2023).
36. Buehler, S. A., Eriksson, P. & Lemke, O. Absorption lookup tables in the radiative transfer model ARTS. *J. Quant. Spectrosc. Radiat. Transf.* **112**, 1559–1567 (2011).
37. Wing, A. A. et al. Radiative–convective equilibrium model intercomparison project. *Geosci. Model Dev.* **11**, 793–813 (2018).
38. Cronin, T. W. On the choice of average solar zenith angle. *J. Atmos. Sci.* **71**, 2994–3003 (2014).
39. L'Ecuyer, T. S. et al. The observed state of the energy budget in the early twenty-first century. *J. Clim.* **28**, 8319–8346 (2015).
40. Coddington, O. et al. *NOAA Climate Data Record (CDR) of Solar Spectral Irradiance (SSI), NRLSSI Version 2.1*. 2017. https://doi.org/10.7289/V53776SW.
41. Roemer, F. E., Buehler, S. A. & Menang, K.*Supplementary data for "How to think about the clear-sky shortwave water vapor feedback"*. Zenodo https://doi.org/10.5281/zenodo.15475114 (2025).
42. Roemer, F. E., Buehler, S. A. & Menang, K.*Supplementary code for "How to think about the clear-sky shortwave water vapor feedback"* Zenodo https://doi.org/10.5281/zenodo.15689635 (2025).

Acknowledgements

This study contributes to the Cluster of Excellence "CLICCS—Climate, Climatic Change, and Society", and to the Center for Earth System Research and Sustainability (CEN) of Universität Hamburg. FR was financially supported by NOAA (award NA20OAR4310375). KM was sponsored by the Alexander von Humboldt Foundation under the program "Humboldt Research Fellowship Programme for Experienced Researchers". We thank the ARTS radiative transfer community for their help with using ARTS. We are grateful to Nadir Jeevanjee for his valuable feedback that helped sharpen the mathematical formulation and analysis of our analytical models. We acknowledge financial support from the Open Access Publication Fund of Universität Hamburg.

Author contributions

F.R and S.B. conceived the study and conceptualized the analytical models, with input from K.M., F.R. conducted the analysis and drafted the manuscript. All authors participated in discussing the results and revising the manuscript.

Funding

Open Access funding enabled and organized by Projekt DEAL.

Competing interests

The authors declare no competing interests.

Additional information

Correspondence and requests for materials should be addressed to Florian E. Roemer.